Mechanics of Materials 139 (2019) 103200

Contents lists available at ScienceDirect

Mechanics of Materials

journal homepage: www.elsevier.com/locate/mechmat

Research paper

Modeling dislocations with arbitrary character angle in face-centered cubic transition metals using the phase-field dislocation dynamics method with full anisotropic elasticity

Shuozhi Xu[*,a], Yanqing Su[b], Irene J. Beyerlein[a,b,c]

[a] California NanoSystems Institute, University of California, Santa Barbara, Santa Barbara, CA 93106-6105, USA
[b] Department of Mechanical Engineering, University of California, Santa Barbara, Santa Barbara CA 93106-5070, USA
[c] Materials Department, University of California, Santa Barbara, Santa Barbara CA 93106-5050, USA

ARTICLE INFO

Keywords:
Elastic anisotropy
Dislocations
Phase-field method

ABSTRACT

In this study, we present a phase-field dislocation dynamics (PFDD) method that includes full anisotropic elasticity. We apply it to calculate the equilibrium core structures of dislocations with arbitrary character angle in eight face-centered cubic transition metals. The calculations investigate the effects of the gradient energy density in the total energy density and the choice of the averaging scheme to determine the isotropic equivalent elastic moduli (i.e., Voigt, Reuss, and Hill). We show that the addition of the gradient energy term increases the intrinsic stacking fault (ISF) widths for the edge and screw dislocations in most of the metals studied here, but decreases the ISF widths for the edge dislocations in four metals: Ir, Ni, Pd, and Rh. The analysis indicates that among the three isotropic averaging schemes, the Voigt isotropic equivalent modulus best predicts the ISF widths of the edge dislocations and the Reuss scheme for the ISF widths of the screw dislocations, compared to the full elastic anisotropy. Finally, a critical character angle ($\sim 60^{\circ}$) is revealed, at which the PFDD simulations with full elastic anisotropy and those with the isotropic Hill average predict the same ISF width. Our work advances the basic understanding of the elastic anisotropic effects on the equilibrium dislocation core structures and can help guide the choice of isotropic averaged moduli.

1. Introduction

Mesoscale modeling of dislocation core structures was traditionally realized via the generalized Peierls-Nabarro (GPN) model (Schoeck, 1994). Similar to the GPN model, the phase-field (PF) dislocation model builds and minimizes the total energy of a dislocated system with respect to a displacement-related continuum field. For face-centered cubic (FCC) crystals, the total energy in GPN models usually consists of two energy terms: the elastic energy and the generalized stacking fault energy (GSFE). Besides these two energy contributions, PF dislocation models usually contain an additional gradient energy, to account for the Shockley partial dislocation cores which naturally form as a result of the unique GSFE landscape in FCC crystals (Xu et al., 2019a). In the last two decades, the PF method was used extensively to simulate equilibrium core structures and dynamics of dislocations.

Different variants of PF dislocation models, while based on the same framework (Wang et al., 2001), have evolved due to optional modelling choices. One PF-based dislocation modeling variant is the PF dislocation dynamics (PFDD) method (Koslowski et al., 2002). To date, PFDD has been used to study a variety of dislocation-mediated plasticity problems, including, but not limited to, core structures of stationary dislocations, dislocation dynamics near a void or in a metallic alloy with spatially varying chemical composition, dislocation nucleation from ledges, as well as slip transfer of a dislocation across a bimetal interface (Beyerlein and Hunter, 2016). Like all other PF-based dislocation models, the PFDD formulation allows a crystal to be treated as an elastic anisotropic medium. However, all previous PFDD simulations, except the most recent ones (Xu et al., 2019b; Su et al., 2019b), assumed linear elastic isotropy by the Voigt average, for the sake of convenience.

On the other hand, it is important to consider full anisotropic elasticity in modeling dislocations (Eshelby et al., 1953; deWit and Koehler, 1959). Both linear elasticity theory and the GPN model found that in FCC metals, approximating an elastic anisotropic medium as an isotropic one results in an underestimation and overestimation of the intrinsic stacking fault (ISF) width associated with the edge and screw

* Corresponding author.
E-mail address: shuozhixu@ucsb.edu (S. Xu).

https://doi.org/10.1016/j.mechmat.2019.103200
Received 16 May 2019; Received in revised form 6 September 2019; Accepted 6 October 2019
Available online 11 October 2019
0167-6636/

dislocations, respectively (Rasmussen et al., 1997; Szajewski et al., 2017). This finding agrees with an analytical study on superdislocations in $L1_0$ TiAl (Song and Chen, 2001). The same conclusion was also reached when PFDD results in Al and Au were compared with another PF dislocation model that incorporates full elastic anisotropy (Xu et al., 2019a). An analytical study of fast-moving dislocations in FCC and body-centered cubic (BCC) metals revealed that the isotropic approximation predicts incorrect line tension of dislocations, especially when the dislocation velocities approach the first shear wave speeds (Blaschke and Szajewski, 2018). In BCC Fe, the experimentally measured equilibrium shapes of dislocation loops (Aubry et al., 2011) and critical stresses to active Frank-Read sources (Fitzgerald et al., 2012) were well reproduced in discrete dislocation dynamics simulations only when the elastic anisotropy was taken into account. In B2 NiAl, the $\{100\} < 100 >$ screw dislocation was found to be stable by isotropic linear elasticity, but unstable by anisotropic linear elasticity, the latter of which agrees with experiments and atomistic simulations (Pasianot et al., 1991; Glatzel et al., 1993). For a zinc-blend $In_xGa_{1-x}As$ layer on a zinc-blend GaAs substrate, there exists a critical layer thickness beyond which a dislocation-free configuration is unstable. Compared with the result obtained using anisotropic elasticity, the critical thickness would be underestimated by 25–40% using isotropic approximation, depending on the value of x (Gosling and Willis, 1994). Taken together, these studies suggest that it is critical to consider full elastic anisotropy in PFDD. In Section 2, we will describe in detail the implementation of full elastic anisotropy, as well as three commonly used isotropic averages (Voigt, Reuss, and Hill), into the PFDD model.

Extending the PFDD method to full elastic anisotropy from elastic isotropy also allows us to explore the consequences of different isotropic averages. Particularly in FCC metals, equilibrium core structures of dislocations greatly influence their mechanical properties and behavior in plastic deformation (Xu et al., 2015; 2016a; 2016b; 2017c; Xu and Chen, 2019). Therefore, in this paper, we study equilibrium core structures of dislocations with arbitrary character angle in eight FCC transition metals, which entail a wide range of Zener anisotropy indices. Previously, applying the GPN model to pure edge and screw dislocations in several FCC metals found that the ratio in the ISF width between anisotropic and Hill-averaged values in different metals scales quasi-linearly with the Zener anisotropy index (Szajewski et al., 2017). However, a systematic study of the effects of the three isotropic averages on both pure- and mixed-type dislocations was lacking. Without understanding how a given isotropic average affects the dislocation core structures, it would be difficult to assess the data in the literature that were usually based on different isotropic averages. Moreover, Szajewski et al. (2017) made two approximations: (i) the GSFE surface was represented by a density functional theory (DFT)-informed truncated Fourier series function and (ii) the elasticity tensor was assumed to be isotropic within the {111} slip plane, i.e., the elasticity tensor was unchanged when the dislocation character angle changed. For the first approximation, the truncated Fourier series function has been found to yield inaccurate GSFE surfaces (and hence spurious dislocation core structures) in FCC Au (Xu et al., 2019a). In this work, the GSFE surfaces for all FCC metals are provided by recent direct DFT calculations (Su et al., 2019a), in lieu of the Fourier series function. For the second approximation, we investigate it in this paper and find the effects to be small (< 3%) for FCC metals, which are highly symmetric. However, the approximation may result in large deviations in predicted dislocation structures in materials with a larger number of independent elastic constants. Thus, full anisotropic elasticity presented in this work allows for better descriptions of dislocations in materials with arbitrary lattice structures.

The paper is structured as follows. We begin with an introduction to the PFDD formulation in Section 2. In Section 3, we build a PFDD simulation cell for a dislocation dipole and determine the gradient energy coefficients for all eight FCC transition metals. The effects of the gradient energy density in the total energy density have been explored in PFDD (Xu et al., 2019a; 2019b) and other PF-based methods (Shen and Wang, 2004; Mianroodi et al., 2016; Pi et al., 2017), but only for 1 or 2 metals in each work. Here, in Section 4.1, we use PFDD to quantify the effects of the gradient energy density in eight FCC metals, wherein oddities are found in some dislocations which are attributed to their unique GSFE landscapes. Then, in Section 4.2, we focus on the effects of different isotropic averages. We find that the Voigt and Reuss averages, respectively, provide the best predictions of the ISF width associated with the edge and screw dislocations for all metals. For the same dislocation in the same metal, the isotropic prediction based on the Hill average sits between those of the Voigt and Reuss averages. In the end, in Section 4.3, PFDD simulations with both full elastic anisotropy and Hill-averaged isotropy are conducted to simulate mixed-type dislocations with arbitrary character angle. We show that there exists a critical character angle at which the two elasticity tensors yield the same ISF width. To our best knowledge, this is the first PF dislocation modeling work that systematically studies dislocations with arbitrary character angle in multiple metals that entail a wide range of Zener anisotropy indices.

2. PFDD formulation

2.1. A brief overview

In this section, we give a brief overview of the PFDD formulation and restrict attention to dislocations within a single {111} slip plane in single-element FCC metals. Three order parameters $\boldsymbol{\phi} = (\phi_1, \phi_2, \phi_3)$ are introduced for the states of slip, respectively, along three different $< 110 >$ directions. $\phi_\alpha = 0$ and 1 represent the unslipped and slipped states, respectively.

Let $\boldsymbol{u}$ represent the displacement field, $\boldsymbol{\beta} = \nabla \boldsymbol{u}$ the distortion field, $\boldsymbol{\epsilon} = \mathrm{sym}\boldsymbol{\beta}$ the strain field, a_0 the lattice parameter, and b the magnitude of the Burgers vector of a perfect dislocation $\boldsymbol{b} = (a_0/2) < 110 >$. The total energy density ψ is the sum of the elastic energy density ψ_{ela}, the GSFE density ψ_{gsf}, and the gradient energy density ψ_{gra} (Xu et al., 2019b), i.e.,

$$\psi(\boldsymbol{\epsilon}, \boldsymbol{\phi}, \nabla\boldsymbol{\phi}) = \psi_{\mathrm{ela}}(\boldsymbol{\epsilon}, \boldsymbol{\phi}) + \psi_{\mathrm{gsf}}(\boldsymbol{\phi}) + \psi_{\mathrm{gra}}(\nabla\boldsymbol{\phi}) \tag{1}$$

where ψ_{gsf} represents the density of energy stored in stacking faults (e.g., ISF) and partial dislocation (e.g., Shockley partial) cores, while ψ_{gra} the density of energy stored in the latter only. In specific,

$$\psi_{\mathrm{ela}}(\boldsymbol{\epsilon}, \boldsymbol{\phi}) = \tfrac{1}{2}[\boldsymbol{\epsilon} - \boldsymbol{\epsilon}^{\mathrm{p}}(\boldsymbol{\phi})]\cdot\boldsymbol{C}[\boldsymbol{\epsilon} - \boldsymbol{\epsilon}^{\mathrm{p}}(\boldsymbol{\phi})] \tag{2}$$

$$\psi_{\mathrm{gsf}}(\boldsymbol{\phi}) = \frac{\gamma_{\mathrm{gsf}}(\boldsymbol{\phi})}{l_{\mathrm{gsf}}} \tag{3}$$

$$\psi_{\mathrm{gra}}(\nabla\boldsymbol{\phi}) = \sum_{\alpha,\beta=1}^{3} \eta_{\mathrm{g0}}^{\alpha\beta}\, \nabla\phi_\alpha \cdot \boldsymbol{N}_{\alpha\beta} \nabla\phi_\beta \tag{4}$$

where $\boldsymbol{C}$ is the stiffness tensor, $\boldsymbol{\epsilon}^{\mathrm{p}} = \mathrm{sym}\boldsymbol{\beta}^{\mathrm{p}}$ is the plastic strain, γ_{gsf} is the GSFE per unit area, l_{gsf} is the interplanar spacing between two adjacent slip planes based on which γ_{gsf} is calculated, and $\eta_{\mathrm{g0}}^{\alpha\beta}$ are the gradient energy coefficients, and

$$\boldsymbol{\beta}^{\mathrm{p}}(\boldsymbol{\phi}) = \sum_{\alpha=1}^{3} \frac{b_\alpha \phi_\alpha}{d_\alpha} \boldsymbol{s}_\alpha \otimes \boldsymbol{n}_\alpha \tag{5}$$

$$\boldsymbol{N}_{\alpha\beta} = \frac{\boldsymbol{b}_\alpha \cdot \boldsymbol{b}_\beta}{d_\alpha d_\beta}[(\boldsymbol{n}_\alpha \cdot \boldsymbol{n}_\beta)\boldsymbol{I} - \boldsymbol{n}_\beta \otimes \boldsymbol{n}_\alpha]. \tag{6}$$

where $\boldsymbol{s}_\alpha$ is the slip direction, $\boldsymbol{n}_\alpha$ is the slip plane unit normal, and $\boldsymbol{b}_\alpha = b_\alpha \boldsymbol{s}_\alpha$ is the slip vector, of the αth order parameter. In the current work of a single slip plane, all slips are confined to the slip plane, and $d_\alpha = d_\beta = l_{\mathrm{gsf}}$.

It follows that the time-dependent Ginzburg-Landau (TDGL) equation is employed to recursively minimize the total energy with respect to each ϕ_α, i.e.,

$$\dot{\phi}_\alpha = m_0 \left[\nabla\cdot\partial_{\nabla\phi_\alpha}\psi_{\text{gra}} - \partial_{\phi_\alpha}(\psi_{\text{ela}} + \psi_{\text{gsf}})\right] \tag{7}$$

where the superposed dot denotes the time derivative and the Ginzburg-Landau coefficient m_0 is non-negative and assumed constant here. Then, to quantify the relaxed dislocation core structures, the continuum disregistry field $\boldsymbol{\zeta}$ is calculated in PFDD as an instantiation of the discrete atomic displacements. The component of $\boldsymbol{\zeta}$ along the i direction is calculated by

$$\zeta_i = \sum_{\alpha=1}^{3} \phi_\alpha \, \boldsymbol{b}_\alpha\cdot\boldsymbol{s}_i \tag{8}$$

where the αth order parameter and i direction lie within the same slip plane.

2.2. Elastic energy

In this section, we focus on the elastic energy because it is the only energy contribution to the total energy that is related to the elastic anisotropy. In PFDD, the goal is to calculate ψ_{ela} at each continuum point located at $\boldsymbol{x}$, as a function of $\boldsymbol{\phi}$ at that point. To better demonstrate the numerical implementation, we rewrite Section 2 as

$$\psi_{\text{ela}}(\boldsymbol{x}) = \frac{1}{2} C_{ijkl}\epsilon^{\text{e}}_{ij}(\boldsymbol{x})\epsilon^{\text{e}}_{kl}(\boldsymbol{x}) \tag{9}$$

and so the elastic energy of the system is

$$\Psi_{\text{ela}} = \int \psi_{\text{ela}}(\boldsymbol{x})\mathrm{d}^3x = \frac{1}{2}\int C_{ijkl}\epsilon^{\text{e}}_{ij}(\boldsymbol{x})\epsilon^{\text{e}}_{kl}(\boldsymbol{x})\mathrm{d}^3x \tag{10}$$

where the elastic strain

$$\epsilon^{\text{e}}_{kl}(\boldsymbol{x}) = \epsilon_{kl}(\boldsymbol{x}) - \epsilon^{\text{p}}_{kl}(\boldsymbol{x}) = \text{sym}\beta_{kl}(\boldsymbol{x}) - \epsilon^{\text{p}}_{kl}(\boldsymbol{x}) = \text{sym}u_{k,l}(\boldsymbol{x}) - \epsilon^{\text{p}}_{kl}(\boldsymbol{x}). \tag{11}$$

On the other hand, in an infinitely large medium without any surface or external body force, the stress equilibrium dictates that (Mura, 1987)

$$u_k(\boldsymbol{x}) = -G_{ki}(\boldsymbol{x})\bigstar(C_{ijmn}\beta^{\text{p}}_{mn}(\boldsymbol{x}))_{,j} \tag{12}$$

where $\star$ denotes the convolution and G_{ki} is the Green's function determined by

$$\hat{G}_{ik}(\boldsymbol{\xi}) = [C_{ijkl}\xi_j\xi_l]^{-1} \tag{13}$$

where $\hat{}$ denotes the Fourier transform and $\boldsymbol{\xi}$ are angular frequencies in the Fourier space.

Substituting Eq. (12) into Eq. (11) yields

$$\begin{aligned}\epsilon^{\text{e}}_{kl}(\boldsymbol{x}) &= -\text{sym}G_{ki,l}(\boldsymbol{x})\bigstar(C_{ijmn}\beta^{\text{p}}_{mn}(\boldsymbol{x}))_{,j} - \epsilon^{\text{p}}_{kl}(\boldsymbol{x}) \\ &= -G_{ki,l}(\boldsymbol{x})\bigstar(C_{ijmn}\epsilon^{\text{p}}_{mn}(\boldsymbol{x}))_{,j} - \epsilon^{\text{p}}_{kl}(\boldsymbol{x})\end{aligned} \tag{14}$$

because of the minor and major symmetries of $\boldsymbol{C}$, i.e.,

$$C_{ijkl} = C_{jikl} = C_{ijlk} = C_{klij}. \tag{15}$$

It is easier to handle the convolution in the Fourier space, suggesting that it is better to calculate Ψ_{ela} in the Fourier space. With this in mind, we resort to the Plancherel theorem and rewrite Eq. (10) as

$$\Psi_{\text{ela}} = \frac{1}{2}\frac{1}{(2\pi)^3}\int C_{ijkl}\hat{\epsilon}^{\text{e}}_{ij}(\boldsymbol{\xi})\hat{\epsilon}^{\text{e}*}_{kl}(\boldsymbol{\xi})\mathrm{d}^3\xi \tag{16}$$

where * denotes the complex conjugate and the principal value of the integral is taken because $\hat{\epsilon}^{\text{e}}_{ij}(\boldsymbol{\xi})$ and $\hat{\epsilon}^{\text{e}*}_{kl}(\boldsymbol{\xi})$ are singular at $\boldsymbol{\xi} = \boldsymbol{0}$. Note that $(2\pi)^3$ would be replaced by unity if $\boldsymbol{\xi}$ were ordinary (i.e., not angular) frequencies.

The elastic strain in the Fourier space for any arbitrary non-zero frequency $\boldsymbol{\xi}$ is

$$\hat{\epsilon}^{\text{e}}_{kl}(\boldsymbol{\xi}) = C_{ijmn}[\hat{G}_{ki}(\boldsymbol{\xi})\xi_j\xi_l - C^{-1}_{klij}]\hat{\epsilon}^{\text{p}}_{mn}(\boldsymbol{\xi}). \tag{17}$$

Derivation of this equation is presented in Appendix A. It follows that

$$\hat{\epsilon}^{\text{e}*}_{kl}(\boldsymbol{\xi}) = C_{ijmn}[\hat{G}_{ki}(\boldsymbol{\xi})\xi_j\xi_l - C^{-1}_{klij}]\hat{\epsilon}^{\text{p}*}_{mn}(\boldsymbol{\xi}). \tag{18}$$

So far we have used indices i, j, k, l, m, n. Equivalently, we may use another set of indices p, q, r, s, u, v and rewrite Eq. (17) as

$$\hat{\epsilon}^{\text{e}}_{rs}(\boldsymbol{\xi}) = C_{pquv}[\hat{G}_{rp}(\boldsymbol{\xi})\xi_q\xi_s - C^{-1}_{rspq}]\hat{\epsilon}^{\text{p}}_{uv}(\boldsymbol{\xi}). \tag{19}$$

Replacing the indices i, j with r, s in Eq. (16) and substituting in Eqs. (18) and (19) yield

$$\begin{aligned}\Psi_{\text{ela}} &= \frac{1}{2}\frac{1}{(2\pi)^3}\int C_{rskl}\hat{\epsilon}^{\text{e}}_{rs}(\boldsymbol{\xi})\hat{\epsilon}^{\text{e}*}_{kl}(\boldsymbol{\xi})\mathrm{d}^3\xi \\ &= \frac{1}{2}\frac{1}{(2\pi)^3}\int \hat{A}_{mnuv}(\boldsymbol{\xi})\hat{\epsilon}^{\text{p}}_{mn}(\boldsymbol{\xi})\hat{\epsilon}^{\text{p}*}_{uv}(\boldsymbol{\xi})\mathrm{d}^3\xi\end{aligned}$$

where

$$\hat{A}_{mnuv}(\boldsymbol{\xi}) = C_{mnuv} - C_{kluv}C_{ijmn}\hat{G}_{ki}(\boldsymbol{\xi})\xi_j\xi_l. \tag{21}$$

Derivation of this equation is presented in Appendix B.

2.3. Full anisotropic elastic tensors

A key ingredient in Eq. (20) is the stiffness matrix C_{ijkl}, which can have up to 21 independent terms. In practice, there is another way to write the matrix form of $\boldsymbol{C}$, if we let $11\to1$, $22\to2$, $33\to3$, $23\to4$, $13\to5$, and $12\to6$, i.e.,

$$\begin{aligned}\boldsymbol{C} &= \begin{bmatrix} C_{1111} & & & & & \\ C_{2211} & C_{2222} & & & & \\ C_{3311} & C_{3322} & C_{3333} & & \text{Symm} & \\ C_{2311} & C_{2322} & C_{2333} & C_{2323} & & \\ C_{3111} & C_{3122} & C_{3133} & C_{3123} & C_{3131} & \\ C_{1211} & C_{1222} & C_{1233} & C_{1223} & C_{1231} & C_{1212} \end{bmatrix} \\ &= \begin{bmatrix} C_{11} & & & & & \\ C_{21} & C_{22} & & & & \\ C_{31} & C_{32} & C_{33} & & \text{Symm} & \\ C_{41} & C_{42} & C_{43} & C_{44} & & \\ C_{51} & C_{52} & C_{53} & C_{54} & C_{55} & \\ C_{61} & C_{62} & C_{63} & C_{64} & C_{65} & C_{66} \end{bmatrix}\end{aligned} \tag{22}$$

In C_{ijkl}, each index can be 1, 2, or 3, with each corresponding to a crystallographic orientation. To ensure full elastic anisotropy, the three orientations, represented by unit vectors $\boldsymbol{e}_1$, $\boldsymbol{e}_2$, $\boldsymbol{e}_3$, must be the ones used by the dislocated system. In FCC metals, e.g., the three orientations are usually $<110>$, $<111>$, and $<112>$. However, the elastic constants obtained by calculations or experiments are usually based on the orientations with the lowest indices, e.g., $\boldsymbol{e}^\dagger_1 = [100]$, $\boldsymbol{e}^\dagger_2 = [010]$, $\boldsymbol{e}^\dagger_3 = [001]$ for cubic materials. Therefore, in cubic materials, the three independent elastic constants $C^\dagger_{11}$, $C^\dagger_{12}$, and $C^\dagger_{44}$ provided in the literature most likely do not equal C_{11}, C_{12}, and C_{44} that should be used in Eq. (22). Let the transformation matrix be $\boldsymbol{K}$, then (Ting, 1996)

$$\boldsymbol{C} = \boldsymbol{K}\boldsymbol{C}^\dagger\boldsymbol{K}^{\text{T}} \tag{23}$$

where

$$\boldsymbol{K} = \begin{bmatrix} \boldsymbol{K}_1 & 2\boldsymbol{K}_2 \\ \boldsymbol{K}_3 & \boldsymbol{K}_4 \end{bmatrix} \tag{24}$$

with

$$\boldsymbol{K}_1 = \begin{bmatrix} \Omega^2_{11} & \Omega^2_{12} & \Omega^2_{13} \\ \Omega^2_{21} & \Omega^2_{22} & \Omega^2_{23} \\ \Omega^2_{31} & \Omega^2_{32} & \Omega^2_{33} \end{bmatrix} \tag{25}$$

$$\boldsymbol{K}_2 = \begin{bmatrix} \Omega_{12}\Omega_{13} & \Omega_{13}\Omega_{11} & \Omega_{11}\Omega_{12} \\ \Omega_{22}\Omega_{23} & \Omega_{23}\Omega_{21} & \Omega_{21}\Omega_{22} \\ \Omega_{32}\Omega_{33} & \Omega_{33}\Omega_{31} & \Omega_{31}\Omega_{32} \end{bmatrix} \tag{26}$$

$$\boldsymbol{K}_3 = \begin{bmatrix} \Omega_{21}\Omega_{31} & \Omega_{22}\Omega_{32} & \Omega_{23}\Omega_{33} \\ \Omega_{31}\Omega_{11} & \Omega_{32}\Omega_{12} & \Omega_{33}\Omega_{13} \\ \Omega_{11}\Omega_{21} & \Omega_{12}\Omega_{22} & \Omega_{13}\Omega_{23} \end{bmatrix} \tag{27}$$

$$\boldsymbol{K}_4 = \begin{bmatrix} \Omega_{22}\Omega_{33}+\Omega_{23}\Omega_{32} & \Omega_{23}\Omega_{31}+\Omega_{21}\Omega_{33} & \Omega_{21}\Omega_{32}+\Omega_{22}\Omega_{31} \\ \Omega_{32}\Omega_{13}+\Omega_{33}\Omega_{12} & \Omega_{33}\Omega_{11}+\Omega_{31}\Omega_{13} & \Omega_{31}\Omega_{12}+\Omega_{32}\Omega_{11} \\ \Omega_{12}\Omega_{23}+\Omega_{13}\Omega_{22} & \Omega_{13}\Omega_{21}+\Omega_{11}\Omega_{23} & \Omega_{11}\Omega_{22}+\Omega_{12}\Omega_{21} \end{bmatrix} \tag{28}$$

where

$$\Omega = \begin{bmatrix} \boldsymbol{e}_1\cdot\boldsymbol{e}_1^\dagger & \boldsymbol{e}_1\cdot\boldsymbol{e}_2^\dagger & \boldsymbol{e}_1\cdot\boldsymbol{e}_3^\dagger \\ \boldsymbol{e}_2\cdot\boldsymbol{e}_1^\dagger & \boldsymbol{e}_2\cdot\boldsymbol{e}_2^\dagger & \boldsymbol{e}_2\cdot\boldsymbol{e}_3^\dagger \\ \boldsymbol{e}_3\cdot\boldsymbol{e}_1^\dagger & \boldsymbol{e}_3\cdot\boldsymbol{e}_2^\dagger & \boldsymbol{e}_3\cdot\boldsymbol{e}_3^\dagger \end{bmatrix}. \tag{29}$$

Similar to 22, there are two equivalent ways to write the compliance tensor $\boldsymbol{S}$ in the matrix form, i.e.,

$$\boldsymbol{S} = \begin{bmatrix} S_{1111} & & & & & \\ S_{2211} & S_{2222} & & & & \\ S_{3311} & S_{3322} & S_{3333} & & \text{Symm} & \\ 2S_{2311} & 2S_{2322} & 2S_{2333} & 4S_{2323} & & \\ 2S_{3111} & 2S_{3122} & 2S_{3133} & 4S_{3123} & 4S_{3131} & \\ 2S_{1211} & 2S_{1222} & 2S_{1233} & 4S_{1223} & 4S_{1231} & 4S_{1212} \end{bmatrix}$$

$$= \begin{bmatrix} S_{11} & & & & & \\ S_{21} & S_{22} & & & & \\ S_{31} & S_{32} & S_{33} & & \text{Symm} & \\ S_{41} & S_{42} & S_{43} & S_{44} & & \\ S_{51} & S_{52} & S_{53} & S_{54} & S_{55} & \\ S_{61} & S_{62} & S_{63} & S_{64} & S_{65} & S_{66} \end{bmatrix}. \tag{30}$$

The following relation holds

$$\boldsymbol{S} = \boldsymbol{C}^{-1} \tag{31}$$

suggesting that

$$C_{ij}S_{jk} = \delta_{ik} \tag{32}$$

where $i, j, k = 1, \ldots, 6$, and

$$C_{mnij}S_{ijkl} = \frac{1}{2}(\delta_{mk}\delta_{nl} + \delta_{ml}\delta_{nk}) \tag{33}$$

where $i, j, k, l, m, n = 1, 2, 3$.

2.4. Isotropic approximations

When the material is assumed elastic isotropic, the transformation matrix $\boldsymbol{K}$ takes no effect, and

$$\boldsymbol{C}^{\text{iso}} = \begin{bmatrix} \lambda+2\mu & & & & & \\ \lambda & \lambda+2\mu & & & & \\ \lambda & \lambda & \lambda+2\mu & & \text{Symm} & \\ & & & \mu & & \\ & & & & \mu & \\ & & & & & \mu \end{bmatrix} \tag{34}$$

where λ and μ are Lamé constants. They are related to each other by the bulk modulus

$$K_{\text{b}} = \lambda + \frac{2}{3}\mu. \tag{35}$$

Multiple isotropic averages have been developed to determine μ and K_{b} based on the elastic constants in $\boldsymbol{C}^\dagger$ (Norris, 1985). In this work, we focus on three most commonly used isotropic averages, proposed respectively by Voigt (1889), Reuss (1929), and Hill (1952). In what follows, quantities obtained by these three averages are denoted by superscripts V, R, and H, respectively.

In the Voigt average, the averaged stiffness tensor is obtained by averaging $\boldsymbol{C}$ over all orientations (Voigt, 1889); as a result,

$$\mu^{\text{V}} = \frac{1}{15}[(C_{11}^\dagger + C_{22}^\dagger + C_{33}^\dagger) - (C_{12}^\dagger + C_{23}^\dagger + C_{13}^\dagger) + 3(C_{44}^\dagger + C_{55}^\dagger + C_{66}^\dagger)] \tag{36}$$

$$K_{\text{b}}^{\text{V}} = \frac{1}{9}[(C_{11}^\dagger + C_{22}^\dagger + C_{33}^\dagger) + 2(C_{12}^\dagger + C_{23}^\dagger + C_{13}^\dagger)]. \tag{37}$$

In the Reuss average, the averaged compliance tensor is obtained by averaging $\boldsymbol{S}$ over all orientations (Reuss, 1929); as a result,

$$\frac{15}{\mu^{\text{R}}} = 4(S_{11}^\dagger + S_{22}^\dagger + S_{33}^\dagger) - 4(S_{12}^\dagger + S_{23}^\dagger + S_{13}^\dagger) + 3(S_{44}^\dagger + S_{55}^\dagger + S_{66}^\dagger) \tag{38}$$

$$\frac{1}{K_{\text{b}}^{\text{R}}} = (S_{11}^\dagger + S_{22}^\dagger + S_{33}^\dagger) + 2(S_{12}^\dagger + S_{23}^\dagger + S_{13}^\dagger) \tag{39}$$

where $\boldsymbol{S}^\dagger = [\boldsymbol{C}^\dagger]^{-1}$. In both Voigt and Reuss averages, Eqs. (35)–(39) are used to form $\boldsymbol{C}^{\text{iso}}$ in Eq. (34). It follows that $\boldsymbol{S}^{\text{iso}} = [\boldsymbol{C}^{\text{iso}}]^{-1}$. It is known that the Voigt and Reuss averages, respectively, provide an upper and a lower bound for the actual effective elastic constants (den Toonder et al., 1999).

Hill (1952) assumed that the arithmetic mean of the Voigt and Reuss averages is a good approximation for the actual elastic constants, i.e.,

$$\boldsymbol{C}^{\text{H}} = \frac{1}{2}(\boldsymbol{C}^{\text{V}} + \boldsymbol{C}^{\text{R}}) \tag{40}$$

$$\boldsymbol{S}^{\text{H}} = \frac{1}{2}(\boldsymbol{S}^{\text{V}} + \boldsymbol{S}^{\text{R}}). \tag{41}$$

However, usually $\boldsymbol{C}^{\text{H}} \neq [\boldsymbol{S}^{\text{H}}]^{-1}$ (Spalthoff et al., 1993).

3. Modeling a dislocation dipole using PFDD

3.1. Simulation set-up

PFDD simulations are carried out using a 3D structured grid, with 256, 8, and 128 grid points in x, y, and z directions, respectively. The simulation cell size was found to be sufficiently large for a dislocation dipole in Al (Xu et al., 2019b). A uniform grid spacing $h_0 = \sqrt{2/3}\,b$ is employed and periodic boundary conditions are applied on all three directions. Let L_x, L_y, and L_z be the edge length of the cell along the x, y, and z directions, respectively. Two dislocation lines lie on the mid-z plane and are separated by $L_x/2$ along the x direction, as illustrated in Fig. 1. The left and right dislocations are placed, respectively, at $L_x/4$ from the left and right periodic boundaries. The attraction between the two dislocations is cancelled out by the attraction between one dislocation and its immediate neighbor in the adjacent periodic image. Hence, the dislocation dipole is in equilibrium.

Initially, an undissociated perfect dislocation dipole with an arbitrary character angle θ is inserted by assigning $\phi_1 = 1$ and $\phi_2 = \phi_3 = 0$ to selected grid points. For edge and screw dislocations, respectively, the crystallographic orientations are $x[1\bar{1}0] - y[11\bar{2}] - z[111]$ and

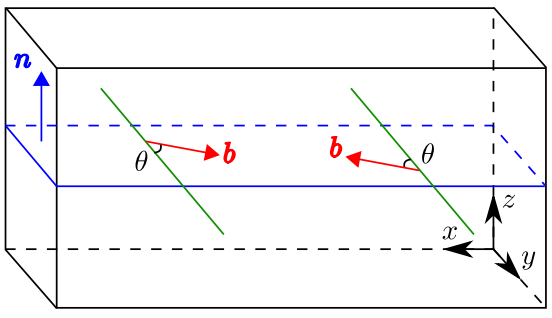

Fig. 1. Simulation box set-up for a mixed-type dislocation dipole.

$x[11\bar{2}] - y[\bar{1}10] - z[111]$. When θ changes, the dislocation lines remain along the y axis but the slip vectors $\boldsymbol{b}_\alpha$ and crystallographic orientations change accordingly. Then, during recursively running the TDGL (Eq. (7)), each dislocation becomes extended. Iterations are terminated when the Euclidean norm of the difference in global vector of each order parameter between successive iterations is smaller than 10^{-4}. The mobility $m_0 = 1$ and the timestep size $\Delta t = 0.02$. In the relaxed dislocation structures, the center of each partial dislocation is determined by projecting the disregistry field onto the Shockley partial dislocation direction (Xu et al., 2019a). The ISF width d is defined as the distance between the centers of two partial dislocations. Based on the numerical resolution, all ISF width values are in $\pm\, b/\sqrt{6}$.

Material parameters needed in the PFDD total energy model include lattice parameter a_0, elastic constants $C_{11}^\dagger$, $C_{12}^\dagger$, and $C_{44}^\dagger$, GSFE surface γ_{gsf}, and gradient energy coefficients $\eta_{g0}^{\alpha\beta}$. In this work, eight FCC transition metals — Ag, Au, Cu, Ir, Ni, Pd, Pt, and Rh — are considered. For each metal, a_0 and γ_{gsf} are based on DFT calculations (Su et al., 2019a). On the other hand, there usually exist relatively large errors (~ 10%) in the elastic constants between DFT calculations and experiments (Zhang et al., 2018). Thus, the elastic constants $C_{11}^\dagger$, $C_{12}^\dagger$, and $C_{44}^\dagger$ are taken from experiments (Warlimont and Martienssen, 2018). Table 1 summarizes some parameters used in PFDD simulations, including two points on the GSFE surface: ISF energy γ_{isf} and unstable stacking fault (USF) energy γ_{usf}.

3.2. Determination of the gradient energy coefficient

As mentioned in Section 2.1, the gradient energy density ψ_{gra} represents the density of energy stored in the Shockley partial dislocations. Prior PFDD simulations in Al and Au (Xu et al., 2019a; 2019b) showed that the predicted dislocation core structures are in better agreement with molecular statics (MS) when ψ_{gra} is included. However, the formulation of ψ_{gra} (Eq. (4)) involves a set of coefficients $\eta_{g0}^{\alpha\beta}$ for which there is no standard method to quantify them (Su et al., 2019b). Regarding characterization, recent work in Al determined non-uniform $\eta_{g0}^{\alpha\beta}$ for edge and screw dislocations by fitting the MS-informed PFDD-based disregistry profiles to MS-based ones (Xu et al., 2019b). Note that in that work, material parameters for PFDD were provided by MS simulations, instead of DFT calculations in the current work. Hence, applying the same approach here would ideally entail characterizing $\eta_{g0}^{\alpha\beta}$ by fitting the PFDD-based disregistry profiles to those from DFT. However, DFT calculations of dislocations are computationally expensive. Among the eight FCC metals, only the screw dislocation in Ni was studied by DFT recently (Tan et al., 2019). Therefore, to approximate values for $\eta_{g0}^{\alpha\beta}$, we compare MS-informed PFDD-based disregistry profiles with MS-based ones for pure edge and screw dislocations. On the other hand, the validity of MS simulations significantly hinges on the robustness of the interatomic potentials (Xu et al., 2017b; Chavoshi et al., 2017; Xu et al., 2017a; 2018; Xu and Su, 2018; Chavoshi and Xu, 2019). For dislocation modeling, it is critical for the interatomic potentials to accurately reproduce the GSFE surface γ_{gsf}. Among the eight FCC metals, suitable potentials only exist for Ag (Williams et al., 2006), Cu (Mishin et al., 2001), and Ni (Foiles and Hoyt, 2006), to the best of our knowledge.

Table 1
Lattice parameter a_0 (in Å), elastic constants $C_{11}^\dagger$, $C_{12}^\dagger$, and $C_{44}^\dagger$ (in GPa), Zener anisotropy index $A_c = 2C_{44}^\dagger/(C_{11}^\dagger - C_{12}^\dagger)$, ISF energy γ_{isf} (in mJ/m^2), and USF energy γ_{usf} (in mJ/m^2) for the eight FCC transition metals used in PFDD simulations. a_0, γ_{isf}, and γ_{usf} are from DFT calculations (Su et al., 2019a), while $C_{11}^\dagger$, $C_{12}^\dagger$, and $C_{44}^\dagger$ are from experiments (Warlimont and Martienssen, 2018).

	Ag	Au	Cu	Ir	Ni	Pd	Pt	Rh
a_0	4.153	4.157	3.634	3.873	3.519	3.942	3.968	3.831
$C_{11}^\dagger$	122	191	169	580	247	221	347	413
$C_{12}^\dagger$	92	162	122	242	153	171	251	194
$C_{44}^\dagger$	45.5	42.2	75.3	256	122	70.8	76.5	184
A_c	3.03	2.91	3.2	1.51	2.6	2.83	1.59	1.68
γ_{isf}	14.49	26.79	41.83	385.87	152.13	135.54	280.87	208.67
γ_{usf}	92.01	76.68	160.52	671.66	300.89	214.93	297.92	475.34
$\gamma_{usf} - \gamma_{isf}$	77.52	49.89	118.69	285.79	148.76	79.39	17.05	266.67

Table 2
For edge (E) and screw (S) dislocations in three FCC metals, d_{MS} (in b) are the ISF widths calculated by MS, and $\eta^{\alpha\beta}$ (in $\mu^V b^2$) are uniform gradient energy coefficients found by PFDD simulations to predict the best agreement with MS.

	Ag	Cu	Ni
d_{MS} (E)	16.25	10.55	6.48
d_{MS} (S)	5.01	2.95	2.67
$\eta_E^{\alpha\beta}$	0.08	0	0.3
$\eta_S^{\alpha\beta}$	0.3	0.1	0.38

It follows that MS simulations are carried out by LAMMPS (Plimpton, 1995) for edge and screw dislocations in Ag, Cu, and Ni. The 3D periodic simulation cells used in MS are similar to that in Fig. 1. In each simulation, an undissociated, perfect dislocation dipole is first created by applying the corresponding isotropic elastic displacement field to all atoms. The dislocated system is then relaxed using the conjugate gradient method. The relaxation step is terminated when one of the following two criteria is satisfied: (i) the change in energy between successive iterations divided by the most recent energy magnitude is less than or equal to 10^{-15} or (ii) the length of the global force vector for all atoms is less than or equal to 10^{-15} eV/Å. The ISF widths, d_{MS}, are summarized in Table 2.

To determine $\eta_{g0}^{\alpha\beta}$ from MS simulations, additional PFDD simulations with full elastic anisotropy and with all material parameters provided by corresponding interatomic potentials are carried out for edge and screw dislocations in Ag, Cu, and Ni. Here, for simplicity, a uniform $\eta_{g0}^{\alpha\beta}$ is used for all sets of $\alpha\beta$ for each dislocation. For each metal, a series of $\eta_{g0}^{\alpha\beta}$, ranging from 0 to $\mu^V b^2$, in increments of $0.1\mu^V b^2$, are considered. Fig. 2 shows the variation in the ISF width d with $\eta_{g0}^{\alpha\beta}$ for the two types of dislocations in three metals. We find that, for edge and screw dislocations, respectively, $\eta_{g0}^{\alpha\beta} = 0.1\mu^V b^2$ and $0.3\mu^V b^2$, on average, provide the best agreement with MS (Table 2). Therefore, these values of $\eta_{g0}^{\alpha\beta}$ will be adopted in all subsequent PFDD simulations for edge and screw dislocations in all eight FCC metals. For mixed-type dislocations with arbitrary character angle θ, a trigonometric interpolation is used (Xu et al., 2019b), i.e.,

$$\eta_{g0}^{\alpha\beta}(\theta) = \frac{1}{2}[\eta_E^{\alpha\beta} + \eta_S^{\alpha\beta} - (\eta_E^{\alpha\beta} - \eta_S^{\alpha\beta})\cos(2\theta)] \tag{42}$$

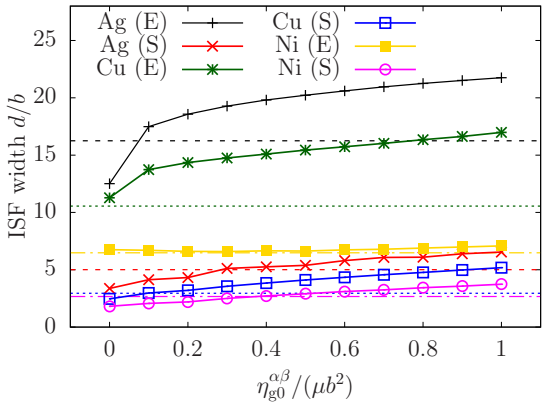

Fig. 2. ISF widths, d, predicted by PFDD, for the edge (E) and screw (S) dislocations in Ag, Cu, and Ni, with respect to the uniform gradient energy coefficient $\eta_{g0}^{\alpha\beta}$. When $\eta_{g0}^{\alpha\beta} = 0$, PFDD simulations are without the gradient energy density ψ_{gra}. MS-based d values are shown as horizontal dashed lines.

Table 3
ISF width d (in b) calculated by PFDD simulations with full elastic anisotropy for edge (E) and screw (S) dislocations in eight FCC metals. Results based on simulations without the gradient energy density ψ_{gra} in the total energy density are denoted by the subscript "ng". Results based on simulations with ψ_{gra} but the stiffness tensor $\boldsymbol{C}$ is based on in-{111}-plane rotated crystallographic orientations are denoted by the superscript *, as described in the text. Based on the numerical resolution, all results are in $\pm\, b/\sqrt{6}$.

	Ag	Au	Cu	Ir	Ni	Pd	Pt	Rh
d (E)	20.17	14.51	12.92	4.71	6.05	3.96	1.91	6.57
d (S)	6.22	3.55	3.63	2.46	2.37	1.52	1.07	3.06
d_{ng} (E)	16.51	13.51	10.49	4.96	6.4	4.45	1.75	7.01
d_{ng} (S)	4.64	2.25	2.56	1.81	1.55	0.88	0.49	2.42
d^* (E)	20.17	14.51	12.92	4.71	6.04	3.96	1.9	6.58
d^* (S)	6.06	3.55	3.49	2.46	2.37	1.52	1.07	3.06

where subscripts "E" and "S" denote the edge and screw dislocations, respectively.

4. Results and discussions

4.1. Edge and screw dislocations: Effects of the gradient energy density

In this section, we focus on edge and screw dislocations using PFDD with full anisotropic elasticity. The ISF widths associated with these dislocations, d, are summarized in Table 3. Results based on PFDD simulations without the gradient energy density ψ_{gra} in the total energy density, denoted by the subscript "ng", are also shown for references. We remark that d_{ng} are what the GPN model would have yielded, if all material parameters are the same (Mianroodi et al., 2016). In previous PF dislocation modeling, introducing the gradient energy increased the ISF widths of both edge and screw dislocations in Al and Au (Mianroodi et al., 2016; Xu et al., 2019a; 2019b) and CoNiRu (Su et al., 2019b), but did not change the ISF width of an edge dislocation in Pd (Shen and Wang, 2004). Nevertheless, a systematic study of the effects of ψ_{gra} in multiple FCC metals is lacking.

Our PFDD simulation results show that, for the same metal, the ISF width of an edge dislocation is larger than that of a screw dislocation, in qualitative agreement with linear elasticity, DFT, and MS. For the same dislocation, $d > d_{ng}$, except the edge dislocations in Ir, Ni, Pd, and Rh. When the gradient energy density is introduced, the Shockley partial dislocation core size increases and the disregistry field is forced to adjust itself. It would be energetically favorable to shrink the ISF area at the expense of elevating the elastic interaction energy between the two partials if the ISF energy γ_{isf} is high and the ISF energy is at a deep well on the GSFE surface, the latter of which may be quantified by a large value of $\gamma_{usf} - \gamma_{isf}$. As shown in Table 1, among the eight metals, (i) Ir, Ni, Pd, Pt, and Rh have the highest γ_{isf}, yet Pt has the smallest value of $\gamma_{usf} - \gamma_{isf}$, (ii) Cu, Ir, Ni, Pd, and Rh have the largest values of $\gamma_{usf} - \gamma_{isf}$ but Cu possesses a low γ_{isf}. These may explain why the ISF width of an edge dislocation decreases upon introducing ψ_{gra} in Ir, Ni, Pd, and Rh.

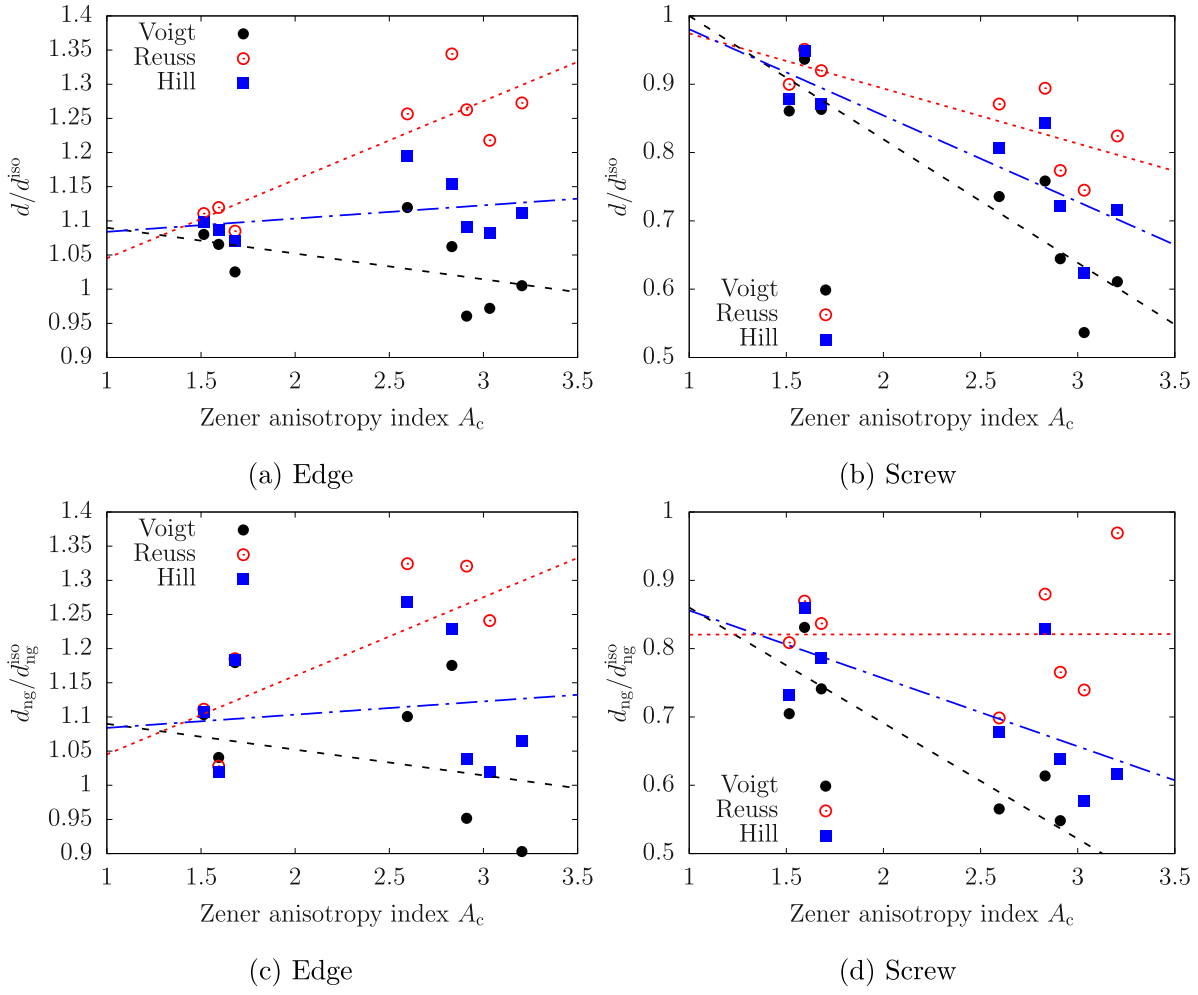

Fig. 3. For edge and screw dislocations in eight FCC metals, the ratio of the elastic anisotropy-based ISF width to elastic isotropy-based ISF width (denoted by the superscript "iso") using the Voigt, Reuss, and Hill averages, respectively. Each dash line shows the linear fit for each isotropic average. In (c–d), the gradient energy density is not included in the total energy density (denoted by the subscript "ng").

Table 4
The ratio of the ISF width predicted by PFDD simulations (d) with elastic anisotropy to that with three isotropic approximations (d^{iso}). Each ratio is an average among all eight FCC metals.

	Voigt	Reuss	Hill
$\overline{d/d^{\text{iso}}}$ (E)	0.966	1.24	1.087
$\overline{d/d^{\text{iso}}}$ (S)	0.574	0.786	0.67

Since all material parameters (except the elastic constants) in the present PFDD simulations are informed by DFT, it is tempting to use DFT data as a benchmark in comparing d and d_{ng}. As mentioned earlier, among the eight FCC metals selected, only the screw dislocation in Ni has been simulated by DFT (Tan et al., 2019), and the corresponding ISF width was $4.82b$, which is larger than our predictions: $d = 2.37b$ and $d_{\text{ng}} = 1.55b$. Note that, however, in measuring the ISF width using DFT results, the centers of the Shockley partial dislocation cores were determined by differential displacement maps and Nye tensor distributions. Neither method is applicable to PF-based disregistry field results. Our previous work showed that different methods to measure the ISF width can lead to results that differ by up to a factor of 3 (Xu et al., 2019a). Nevertheless, since d is closer to the DFT prediction than d_{ng}, it is suggested that the gradient energy density should be included in the total energy density, at least for the screw dislocation in Ni.

As mentioned in Section 1, in their GPN-based work, Szajewski et al. (2017) assumed the elasticity tensor to be isotropic within the {111} slip plane. To validate this approximation, we redo all ψ_{gra}-included PFDD calculations in this section but with the stiffness tensor $\boldsymbol{C}$ based on crystallographic orientations that are rotated by 90° within the {111} plane. In specific, $\boldsymbol{C}$ for edge and screw dislocations, respectively, are based on $x[11\bar{2}] - y[\bar{1}10] - z[111]$ and $x[1\bar{1}0] - y[11\bar{2}] - z[111]$ orientations. Results are denoted by the superscript * and presented in Table 3. Comparing d and d^*, we find that the errors caused by this approximation are indeed small, less than 3%.

4.2. Edge and screw dislocations: Effects of different isotropic averages

In this section, we explore the effects of the three commonly used elastic isotropic averages — Voigt, Reuss, and Hill — on the core structures of edge and screw dislocations. The ISF widths based on the isotropic averages are collectively denoted as d^{iso}. The ratios d/d^{iso} for the three isotropic averages, presented in Fig. 3(a–b), are based on PFDD simulations with the gradient energy density ψ_{gra} included in the total energy density. The same pattern discussed below is also found in results based on PFDD simulations without ψ_{gra}. Those results are presented in Fig. 3(c–d).

First, using the same average, the ratio in the ISF width quasi-linearly scales with the Zener anisotropy index $A_{\text{c}} = 2C_{44}^{\dagger}/(C_{11}^{\dagger} - C_{12}^{\dagger})$ of the material. Second, almost all isotropic averages underestimate and overestimate, respectively, the ISF widths associated with the edge and screw dislocations, i.e.,

$$d > d^{\text{iso}} \quad \text{for edge dislocation} \tag{43}$$

$$d < d^{\text{iso}} \quad \text{for screw dislocation} \tag{44}$$

Both findings qualitatively agree with previous GPN-based simulations, which neglected ψ_{gra} (Szajewski et al., 2017). This agreement, which in part validates our numerical implementations, is expected because including ψ_{gra} does not affect the variation in elastic energy with different isotropic averages. Note that the ratio d/d^{iso} is farther away from unity for the screw dislocations than for the edge dislocations, as a result of the generally smaller ISF widths associated with the former than those with the latter.

What was lacking in the previous GPN-based simulations was a systematic study of the effects of the three isotropic averages. Here, we find that, for the same dislocation, the Voigt average always results in a larger ISF width than the Reuss average, with the Hill average prediction in-between, i.e.,

$$d^{\text{V}} > d^{\text{H}} > d^{\text{R}} \tag{45}$$

As mentioned earlier, the Voigt and Reuss averages provide an upper and a lower bound for the actual effective elastic constants, respectively. On the one hand, adopting different stiffness tensors $\boldsymbol{C}$ only affects the elastic energy Ψ_{ela}. On the other hand, upon energy minimization, Ψ_{ela} always needs to balance the other two energy contributions. Thus, for the same displacement field $\boldsymbol{u}$, Ψ_{ela} is the same regardless of what form $\boldsymbol{C}$ takes. Since the Voigt average yields a stiffer material, the total elastic strain will become smaller, according to Eq. (10). In the meantime, the total plastic strain in the system remains almost unchanged because the total amount of slips does not change with $\boldsymbol{C}$. As such, Eq. (11) suggests that the total strain will become smaller. For this to occur, $\boldsymbol{u}$ will become smoother, resulting in a larger ISF width.

Comparing Eqs. (43) and (45), one sees that the Voigt average is the best among all three isotropic approximations to predict the ISF width associated with an edge dislocation. Similarly, comparing Eqs. (44) and (45) suggests that the Reuss average provides the best prediction of the ISF width of a screw dislocation. These are validated by the averaged ratios, $\overline{d/d^{\text{iso}}}$, presented in Table 4. We remark that the main uncertainties in PFDD simulations lie in determining the model parameters, including the GSFE surfaces and the gradient energy coefficients, which do not influence the elastic energies. Hence, the main conclusions drawn in this section is likely sound.

4.3. Mixed-type dislocations: Effects of the isotropic Hill average

The preceding two sections analyzed the effects of both the gradient energy density ψ_{gra} and different isotropic averages on edge and screw dislocations. In this section, we investigate mixed-type dislocations with arbitrary character angle. Our earlier work in Al found that the effects of ψ_{gra} are the same for pure- and mixed-type dislocations (Xu et al., 2019b), so we will not study the effects of ψ_{gra} here and will include ψ_{gra} in the total energy density in all subsequent PFDD simulations. In addition, earlier analytical study showed that, among the three isotropic averages, the Hill average retains the bulk modulus, while the Voigt and Reuss averages overestimates and underestimates it, respectively (Szajewski et al., 2017). Hence, in what follows, we compare results based on elastic anisotropy and the isotropic Hill average.

The ISF widths obtained from PFDD simulations are summarized in Fig. 4. For the same metal, the ISF width monotonically increases with the character angle θ, in agreement with elasticity theory. As discussed earlier, for the edge dislocation ($\theta = 90°$), $d > d^{\text{H}}$, and for the screw dislocation ($\theta = 0°$), $d < d^{\text{H}}$. Thus, there must be a mixed dislocation with a critical character angle θ at which elastic anisotropy and Hill average yield the same ISF width, i.e., $d/d^{\text{H}} = 1$.

Fig. 5 shows that this critical angle does exist. However, it is difficult to directly identify it because the ratio d/d^{H} does not change monotonically with θ. So we resort to obtain approximated values. Recall that because of the numerical resolution, $\sqrt{2/3}\,b$, all ISF width values are in $\pm\, b/\sqrt{6}$. For PFDD simulations with elastic anisotropy (the first two rows in Table 3), the averaged d among all 16 pure-type dislocations is $5.9175b$. Then, on average, the ratios d/d^{H} are in $\pm\, 1/(5.9175 \times \sqrt{6}) = \pm 0.069$. It follows that, for each metal, all character angles corresponding to the bounded region $0.931 < d/d^{\text{H}} < 1.069$ in Fig. 5 are averaged. The averaged values are taken as the approximated critical angles, and are summarized in Table 5. The critical angles are between 57.5° and 62°, and on average $\sim 60°$. This suggests that, for a given dislocation, the more its character angle deviates from 60°, the larger the error in the ISF width resulting from the Hill average. As mentioned early, the ISF width of the edge dislocation

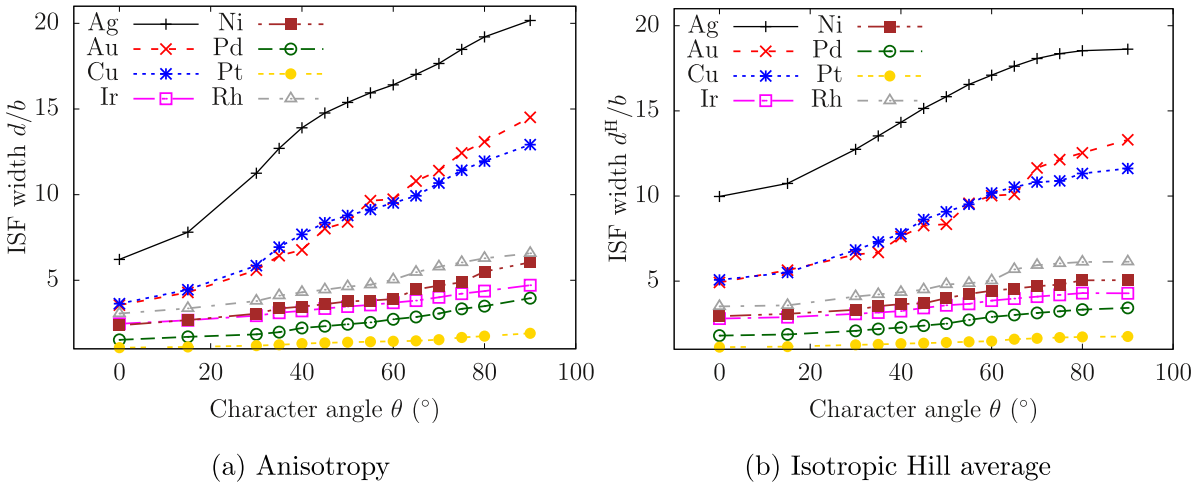

Fig. 4. For dislocations with arbitrary character angle θ in eight FCC metals, the ISF widths predicted by PFDD simulations with elastic anisotropy, d, and those with the isotropic Hill average, d^H.

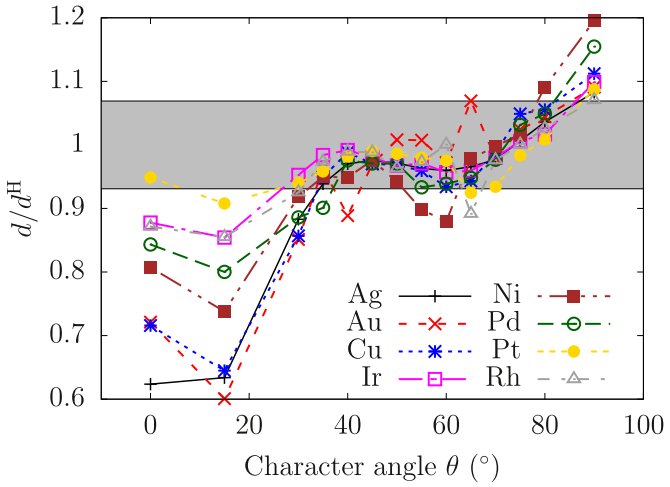

Fig. 5. For dislocations with arbitrary character angle θ in eight FCC metals, the ratio in the ISF width between the elastic anisotropy-based values d and the Hill average-based values d^H. The shaded region bounded within $0.931 < d/d^H < 1.069$ represents possible numerical errors in calculating the ratios.

Table 5
For all eight FCC metals, the critical character angles (in °) at which PFDD simulations with elastic anisotropy and those with the isotropic Hill average yield the same ISF width.

Ag	Au	Cu	Ir	Ni	Pd	Pt	Rh
60	62	60	57.5	57.5	60	57.5	59.58

(90°) is less affected by the isotropic approximation than the screw dislocation (0°).

5. Conclusions

In this paper, we first extend the PFDD method from isotropic elasticity to full anisotropic elasticity. Numerical implementations are detailed in Section 2. Then, in Sections 3 and 4, we apply the enhanced approach to systematically study the effects of the gradient energy density and different isotropic averages (Voigt, Reuss, and Hill) on core structures of pure- and mixed-type dislocations in eight FCC transition metals. Key conclusions are as follows:

1. Among all 16 pure-type dislocations in eight FCC metals, adding the gradient energy density ψ_{ng} to the total energy density increases the ISF widths d associated with 12 dislocations, but decreases d of the edge dislocations in Ir, Ni, Pd, and Rh. This may be attributed to the GSFE landscapes associated with these four metals.
2. Using the same isotropic average, the ratio in the ISF width between the anisotropy-based value and the isotropy-based one quasi-linearly scales with the Zener anisotropy index of the material. In addition, almost all isotropic averages underestimate and overestimate, respectively, the ISF widths associated with the edge and screw dislocations. The two findings agree with previous GPN-based simulations (Szajewski et al., 2017).
3. Among the three isotropic averages, for the same dislocation, the Voigt and Reuss averages always predict the widest and narrowest ISFs, respectively, while the Hill average values are in-between. This is likely an outcome of the stiffer and softer material yielded by the Voigt and Reuss averages, respectively. As a result, among the three isotropic averages, the Voigt and Reuss averages best predict the ISF widths associated with the edge and screw dislocations, respectively.
4. For all eight FCC metals, a critical angle, $\sim 60^\circ$, is identified at which the elastic anisotropy and isotropic Hill average yield the same ISF width.

Acknowledgments

We thank Dr. Abigail Hunter, Dr. Jaber R. Mianroodi, Dr. Chunfeng Cui, and Ms. Xiaoyao Peng for helpful discussions. The work of S.X. was supported in part by the Elings Prize Fellowship in Science offered by the California NanoSystems Institute on the UC Santa Barbara campus. The authors gratefully acknowledge support from the Office of Naval Research under contract ONR BRC Grant N00014-18-1-2392. Use was made of computational facilities purchased with funds from the National Science Foundation (CNS-1725797) and administered by the Center for Scientific Computing (CSC). The CSC is supported by the California NanoSystems Institute and the Materials Research Science and Engineering Center (MRSEC; NSF DMR 1720256) at UC Santa Barbara. This work used the Extreme Science and Engineering Discovery Environment (XSEDE), which is supported by National Science Foundation grant number ACI-1053575.

Appendix A. Derivation of Eq. (17)

First, recall these identities:

$$\mathcal{F}[f(x)\bigstar g(x)] = \mathcal{F}[f(x)]\cdot\mathcal{F}[g(x)] \tag{A.1}$$

$$\mathcal{F}[f'(x)] = \sqrt{-1}\xi\hat{f}(\xi) \tag{A.2}$$

$$C_{mnij}C^{-1}_{ijkl} = \delta_{mk}\delta_{nl} \tag{A.3}$$

where $\mathcal{F}$ conducts the Fourier transform, f and g are functions of x, δ_{mk} and δ_{nl} are the Kronecker delta. Then,

$$\begin{aligned}
\hat{\epsilon}^{e}_{kl}(\boldsymbol{\xi}) = \mathcal{F}[\epsilon^{e}_{kl}(\boldsymbol{x})] &= \mathcal{F}[-G_{ki,l}(\boldsymbol{x})\bigstar(C_{ijmn}\epsilon^{p}_{mn}(\boldsymbol{x}))_{,j} - \epsilon^{p}_{kl}(\boldsymbol{x})] \\
&= -\mathcal{F}[G_{ki,l}(\boldsymbol{x})\bigstar(C_{ijmn}\epsilon^{p}_{mn}(\boldsymbol{x}))_{,j}] - \hat{\epsilon}^{p}_{kl}(\boldsymbol{\xi}) \\
&= -\mathcal{F}[G_{ki,l}(\boldsymbol{x})]\cdot\mathcal{F}[(C_{ijmn}\epsilon^{p}_{mn}(\boldsymbol{x}))_{,j}] - \hat{\epsilon}^{p}_{kl}(\boldsymbol{\xi}) \\
&= -[\sqrt{-1}\xi_l\hat{G}_{ki}(\boldsymbol{\xi})]\cdot[\sqrt{-1}\xi_j C_{ijmn}\hat{\epsilon}^{p}_{mn}(\boldsymbol{\xi})] - \hat{\epsilon}^{p}_{kl}(\boldsymbol{\xi}) \\
&= \hat{G}_{ki}(\boldsymbol{\xi})\xi_j\xi_l C_{ijmn}\hat{\epsilon}^{p}_{mn}(\boldsymbol{\xi}) - \hat{\epsilon}^{p}_{kl}(\boldsymbol{\xi}) \\
&= \hat{G}_{ki}(\boldsymbol{\xi})\xi_j\xi_l C_{ijmn}\hat{\epsilon}^{p}_{mn}(\boldsymbol{\xi}) - \delta_{mk}\delta_{nl}\hat{\epsilon}^{p}_{mn}(\boldsymbol{\xi}) \\
&= \hat{G}_{ki}(\boldsymbol{\xi})\xi_j\xi_l C_{ijmn}\hat{\epsilon}^{p}_{mn}(\boldsymbol{\xi}) - C_{ijmn}C^{-1}_{klij}\hat{\epsilon}^{p}_{mn}(\boldsymbol{\xi}) \\
&= C_{ijmn}[\hat{G}_{ki}(\boldsymbol{\xi})\xi_j\xi_l - C^{-1}_{klij}]\hat{\epsilon}^{p}_{mn}(\boldsymbol{\xi}).
\end{aligned} \tag{A.4}$$

Appendix B. Derivation of Eq. (21)

First, we substitute Eqs. (18) and (19) into the first integral in Eq. (20). Second, we compare the result with the second integral in Eq. (20), yielding

$$\begin{aligned}
\hat{A}_{mnuv}(\boldsymbol{\xi}) &= C_{rskl}C_{pquv}C_{ijmn}[\hat{G}_{rp}(\boldsymbol{\xi})\xi_q\xi_s - C^{-1}_{rspq}][\hat{G}_{ki}(\boldsymbol{\xi})\xi_j\xi_l - C^{-1}_{klij}] \\
&= C_{rskl}C_{pquv}C_{ijmn}[\hat{G}_{rp}(\boldsymbol{\xi})\xi_q\xi_s\hat{G}_{ki}(\boldsymbol{\xi})\xi_j\xi_l \\
&\quad - C^{-1}_{rspq}\hat{G}_{ki}(\boldsymbol{\xi})\xi_j\xi_l - \hat{G}_{rp}(\boldsymbol{\xi})\xi_q\xi_s C^{-1}_{klij} + C^{-1}_{rspq}C^{-1}_{klij}]
\end{aligned} \tag{B.1}$$

Then, with the help of Eq. (13), the first term becomes

$$\begin{aligned}
C_{rskl}C_{pquv}C_{ijmn}\hat{G}_{rp}(\boldsymbol{\xi})\xi_q\xi_s\hat{G}_{ki}(\boldsymbol{\xi})\xi_j\xi_l &= C_{rskl}C_{pquv}C_{ijmn}\hat{G}_{rp}(\boldsymbol{\xi})\xi_q\xi_s[C_{khit}\xi_h\xi_t]^{-1}\xi_j\xi_l \\
&= C_{rskl}C_{pquv}C_{ijmn}\hat{G}_{rp}(\boldsymbol{\xi})\xi_q\xi_s C^{-1}_{khit}[\xi_h\xi_t]^{-1}\xi_j\xi_l \\
&= C_{rskl}C_{pquv}C_{ijmn}\hat{G}_{rp}(\boldsymbol{\xi})\xi_q\xi_s C^{-1}_{khit}\delta_{ij}\delta_{hl} \\
&= C_{rskl}C_{pquv}C_{ijmn}\hat{G}_{rp}(\boldsymbol{\xi})\xi_q\xi_s C^{-1}_{klij}
\end{aligned} \tag{B.2}$$

which then cancels out the third term.

It follows that, with the help of Eq. (A.3), the second and the fourth terms, respectively, become

$$C_{rskl}C_{pquv}C_{ijmn}C^{-1}_{rspq}\hat{G}_{ki}(\boldsymbol{\xi})\xi_j\xi_l = \delta_{kp}\delta_{lq}C_{pquv}C_{ijmn}\hat{G}_{ki}(\boldsymbol{\xi})\xi_j\xi_l = C_{kluv}C_{ijmn}\hat{G}_{ki}(\boldsymbol{\xi})\xi_j\xi_l \tag{B.3}$$

$$C_{rskl}C_{pquv}C_{ijmn}C^{-1}_{rspq}C^{-1}_{klij} = \delta_{kp}\delta_{lq}\delta_{mk}\delta_{nl}C_{pquv} = C_{mnuv}. \tag{B.4}$$

As a result,

$$\hat{A}_{mnuv}(\boldsymbol{\xi}) = C_{mnuv} - C_{kluv}C_{ijmn}\hat{G}_{ki}(\boldsymbol{\xi})\xi_j\xi_l. \tag{B.5}$$

References

Aubry, S., Fitzgerald, S.P., Dudarev, S.L., Cai, W., 2011. Equilibrium shape of dislocation shear loops in anisotropic α-Fe. Modelling Simul. Mater. Sci. Eng. 19 (6), 065006. https://doi.org/10.1088/0965-0393/19/6/065006.

Beyerlein, I.J., Hunter, A., 2016. Understanding dislocation mechanics at the mesoscale using phase field dislocation dynamics. Philos. Trans. R. Soc. A 374 (2066), 20150166. https://doi.org/10.1098/rsta.2015.0166.

Blaschke, D.N., Szajewski, B.A., 2018. Line tension of a dislocation moving through an anisotropic crystal. Philos. Mag. 98 (26), 2397–2424. https://doi.org/10.1080/14786435.2018.1489152.

Chavoshi, S.Z., Xu, S., 2019. Nanoindentation/scratching at finite temperatures: Insights from atomistic-based modeling. Prog. Mater. Sci. 100, 1–20. https://doi.org/10.1016/j.pmatsci.2018.09.002.

Chavoshi, S.Z., Xu, S., Goel, S., 2017. Addressing the discrepancy of finding the equilibrium melting point of silicon using molecular dynamics simulations. Proc. R. Soc. A 473 (2202), 20170084. https://doi.org/10.1098/rspa.2017.0084.

deWit, G., Koehler, J.S., 1959. Interaction of dislocations with an applied stress in anisotropic crystals. Phys. Rev. 116 (5), 1113–1120. https://doi.org/10.1103/PhysRev.116.1113.

Eshelby, J.D., Read, W.T., Shockley, W., 1953. Anisotropic elasticity with applications to dislocation theory. Acta Metall. 1 (3), 251–259. https://doi.org/10.1016/0001-6160(53)90099-6.

Fitzgerald, S.P., Aubry, S., Dudarev, S.L., Cai, W., 2012. Dislocation dynamics simulation of Frank-Read sources in anisotropic α-Fe. Modelling Simul. Mater. Sci. Eng. 20 (4), 045022. https://doi.org/10.1088/0965-0393/20/4/045022.

Foiles, S.M., Hoyt, J., 2006. Computation of grain boundary stiffness and mobility from boundary fluctuations. Acta Mater. 54 (12), 3351–3357. https://doi.org/10.1016/j.actamat.2006.03.037.

Glatzel, U., Forbes, K.R., Nix, W.D., 1993. Dislocation energies for an anisotropic cubic crystal calculations and observations for NiAl. Philos. Mag. A 67 (2), 307–323. https://doi.org/10.1080/01418619308207160.

Gosling, T.J., Willis, J.R., 1994. The energy of arrays of dislocations in an anisotropic half-

space. Philos. Mag. A 69 (1), 65–90. https://doi.org/10.1080/01418619408242211.
Hill, R., 1952. The elastic behaviour of a crystalline aggregate. Proc. Phys. Soc. A 65 (5), 349–354. https://doi.org/10.1088/0370-1298/65/5/307.
Koslowski, M., Cuitiño, A.M., Ortiz, M., 2002. A phase-field theory of dislocation dynamics, strain hardening and hysteresis in ductile single crystals. J. Mech. Phys. Solids 50 (12), 2597–2635. https://doi.org/10.1016/S0022-5096(02)00037-6.
Mianroodi, J.R., Hunter, A., Beyerlein, I., Svendsen, B., 2016. Theoretical and computational comparison of models for dislocation dissociation and stacking fault / core formation in fcc crystals. J. Mech. Phys. Solids 95, 719–741.
Mishin, Y., Mehl, M.J., Papaconstantopoulos, D.A., Voter, A.F., Kress, J.D., 2001. Structural stability and lattice defects in copper: *Ab initio*, tight-binding, and embedded-atom calculations. Phys. Rev. B 63 (22), 224106. https://doi.org/10.1103/PhysRevB.63.224106.
Mura, T., 1987. Micromechanics of Defects in Solids, second. Springer, Dordrecht, Netherlands; Boston: Hingham, MA, USA.
Norris, A.N., 1985. A differential scheme for the effective moduli of composites. Mech. Mater. 4 (1), 1–16. https://doi.org/10.1016/0167-6636(85)90002-X.
Pasianot, R., Farkas, D., Savino, E.J., 1991. Dislocation core structure in ordered intermetallic alloys. J. Phys. III France 1 (6), 997–1014. https://doi.org/10.1051/jp3:1991169.
Pi, Z.P., Fang, Q.H., Jiang, C., Liu, B., Liu, Y., Wen, P.H., Liu, Y.W., 2017. Stress dependence of the dislocation core structure and loop nucleation for face-centered-cubic metals. Acta Mater. 131, 380–390. https://doi.org/10.1016/j.actamat.2017.04.019.
Plimpton, S., 1995. Fast parallel algorithms for short-range molecular dynamics. J. Comput. Phys. 117 (1), 1–19. https://doi.org/10.1006/jcph.1995.1039.
Rasmussen, T., Jacobsen, K.W., Leffers, T., Pedersen, O.B., 1997. Simulations of the atomic structure, energetics, and cross slip of screw dislocations in copper. Phys. Rev. B 56 (6), 2977–2990. https://doi.org/10.1103/PhysRevB.56.2977.
Reuss, A., 1929. Berechnung der Fließgrenze von Mischkristallen auf Grund der Plastizitätsbedingung für Einkristalle. Z. Angew, Math. Mech. 9 (1), 49–58. https://doi.org/10.1002/zamm.19290090104.
Schoeck, G., 1994. The generalized Peierls-Nabarro model. Philos. Mag. A 69 (6), 1085–1095. https://doi.org/10.1080/01418619408242240.
Shen, C., Wang, Y., 2004. Incorporation of γ-surface to phase field model of dislocations: simulating dislocation dissociation in fcc crystals. Acta Mater. 52, 683–691. https://doi.org/10.1016/j.actamat.2003.10.014.
Song, X.P., Chen, G.L., 2001. Effect of elastic anisotropy on the dissociation widths of superdislocations in TiAl. Mater. Lett. 48 (5), 273–280. https://doi.org/10.1016/S0167-577X(00)00315-3.
Spalthoff, P., Wunnike, W., Nauer-Gerhard, C., Bunge, H.J., Schneider, E., 1993. Determination of the elastic tensor of a textured low-carbon steel. Textures Microstruct. 21 (1), 3–16. https://doi.org/10.1155/TSM.21.3.
Su, Y., Xu, S., Beyerlein, I.J., 2019. Density functional theory calculations of generalized stacking fault energy surfaces for eight face-centered cubic transition metals. J. Appl. Phys. 126 (10), 105112. https://doi.org/10.1063/1.5115282.
Su, Y., Xu, S., Beyerlein, I.J., 2019. *Ab initio*-informed phase-field modeling of dislocation core structures in equal-molar CoNiRu multi-principal element alloys. Modelling Simul. Mater. Sci. Eng. 27 (8), 084001. https://doi.org/10.1088/1361-651X/ab3b62.
Szajewski, B.A., Hunter, A., Luscher, D.J., Beyerlein, I.J., 2017. The influence of anisotropy on the core structure of Shockley partial dislocations within FCC materials. Modelling Simul. Mater. Sci. Eng. 26 (1), 015010. https://doi.org/10.1088/1361-651X/aa9758.
Tan, A.M.Z., Woodward, C., Trinkle, D.R., 2019. Dislocation core structures in Ni-based superalloys computed using a density functional theory based flexible boundary condition approach. Phys. Rev. Mater. 3 (3), 033609. https://doi.org/10.1103/PhysRevMaterials.3.033609.
Ting, T.C.T., 1996. Anisotropic Elasticity: Theory and Applications, 1. Oxford University Press, New York.
den Toonder, J.M.J., Dommelen, J.A.W.v., Baaijens, F.P.T., 1999. The relation between single crystal elasticity and the effective elastic behaviour of polycrystalline materials: theory, measurement and computation. Modelling Simul. Mater. Sci. Eng. 7 (6), 909–928. https://doi.org/10.1088/0965-0393/7/6/301.
Voigt, W., 1889. Ueber die Beziehung zwischen den beiden Elasticitätsconstanten isotroper Körper. Ann. Phys. 274 (12), 573–587. https://doi.org/10.1002/andp.18892741206.
Wang, Y.U., Jin, Y.M., Cuitiño, A.M., Khachaturyan, A.G., 2001. Nanoscale phase field microelasticity theory of dislocations: model and 3d simulations. Acta Mater. 49 (10), 1847–1857. https://doi.org/10.1016/S1359-6454(01)00075-1.
Springer Handbook of Materials Data. In: Warlimont, H., Martienssen, W. (Eds.), second. Springer International Publishing.
Williams, P.L., Mishin, Y., Hamilton, J.C., 2006. An embedded-atom potential for the Cu and Ag system. Modelling Simul. Mater. Sci. Eng. 14 (5), 817–833. https://doi.org/10.1088/0965-0393/14/5/002.
Xu, S., Che, R., Xiong, L., Chen, Y., McDowell, D.L., 2015. A quasistatic implementation of the concurrent atomistic-continuum method for FCC crystals. Int. J. Plast. https://doi.org/10.1016/j.ijplas.2015.05.007.
Xu, S., Chen, X., 2019. Modeling dislocations and heat conduction in crystalline materials: atomistic/continuum coupling approaches. Int. Mater. Rev. 64 (7), 407–438. https://doi.org/10.1080/09506608.2018.1486358.
Xu, S., Mianroodi, J.R., Hunter, A., Beyerlein, I.J., Svendsen, B., 2019. Phase-field-based calculations of the disregistry fields of static extended dislocations in FCC metals. Philos. Mag. 99 (11), 1400–1428. https://doi.org/10.1080/14786435.2019.1582850.
Xu, S., Smith, L., Mianroodi, J.R., Hunter, A., Svendsen, B., Beyerlein, I.J., 2019. A comparison of different continuum approaches in modeling mixed-type dislocations in Al. Modelling Simul. Mater. Sci. Eng. 27 (7), 074004. https://doi.org/10.1088/1361-651X/ab2d16.
Xu, S., Startt, J.K., Payne, T.G., Deo, C.S., McDowell, D.L., 2017. Size-dependent plastic deformation of twinned nanopillars in body-centered cubic tungsten. J. Appl. Phys. 121 (17), 175101. https://doi.org/10.1063/1.4982754.
Xu, S., Su, Y., 2018. Dislocation nucleation from symmetric tilt grain boundaries in body-centered cubic vanadium. Phys. Lett. A 382 (17), 1185–1189. https://doi.org/10.1016/j.physleta.2018.03.002.
Xu, S., Su, Y., Chavoshi, S.Z., 2018. Deformation of periodic nanovoid structures in Mg single crystals. Mater. Res. Express 5 (1), 016523. https://doi.org/10.1088/2053-1591/aaa678.
Xu, S., Xiong, L., Chen, Y., McDowell, D.L., 2016. An analysis of key characteristics of the Frank-Read source process in FCC metals. J. Mech. Phys. Solids 96, 460–476. https://doi.org/10.1016/j.jmps.2016.08.002.
Xu, S., Xiong, L., Chen, Y., McDowell, D.L., 2016. Sequential slip transfer of mixed-character dislocations across Σ3 coherent twin boundary in FCC metals: a concurrent atomistic-continuum study. npj Comput. Mater. 2, 15016. https://doi.org/10.1038/npjcompumats.2015.16.
Xu, S., Xiong, L., Chen, Y., McDowell, D.L., 2017. Comparing EAM potentials to model slip transfer of sequential mixed character dislocations across two symmetric tilt grain boundaries in Ni. JOM 69 (5), 814–821. https://doi.org/10.1007/s11837-017-2302-1.
Xu, S., Xiong, L., Chen, Y., McDowell, D.L., 2017. Validation of the concurrent atomistic-continuum method on screw dislocation/stacking fault interactions. Crystals 7 (5), 120. https://doi.org/10.3390/cryst7050120.
Zhang, G.-X., Reilly, A.M., Tkatchenko, A., Scheffler, M., 2018. Performance of various density-functional approximations for cohesive properties of 64 bulk solids. New J. Phys. 20 (6), 063020. https://doi.org/10.1088/1367-2630/aac7f0.